

High and Low-Speed Streaks in Turbulent Wedge Spreading

Alexandre R. Berger¹† and Edward B. White¹

¹Department of Aerospace Engineering, Texas A&M University,
College Station, Texas 77843, USA

(Received xx; revised xx; accepted xx)

Boundary-layer transition triggered by a roughness element generates a turbulent wedge that spreads laterally as the flow proceeds downstream. The spreading half angle is about 6° in zero-pressure-gradient flows regardless of Reynolds number and roughness shape. Recent simulations and experiments have sought to explain the lateral-spreading mechanism and have observed high- and low-speed streaks along the flanks of the wedge that appear central to the spreading process. To better elucidate the role of streaks, a naphthalene flow-visualization survey and hotwire measurements are conducted over a wider range of Reynolds numbers and a longer streamwise domain than previous experiments. The results reconfirm the spreading half angle is insensitive to Reynolds numbers based on roughness location, $Re_{x,k}$, and roughness height, Re_{kk} . When made nondimensional by the unit Reynolds number, the distance from the roughness to the effective origin of the turbulent wedge and to the first high-speed flanking streaks depends on Re_{kk} but not $Re_{x,k}$. The distance between the first and second high-speed streaks is also observed to depend on Re_{kk} . In spite of a long measurement domain, third streaks are not observed and it remains unknown whether subsequent streak-to-streak distances collapse to a universal value. The reason downstream streaks are not observed may be low-frequency meandering of streak structures. Hotwire measurements confirm breakdown to turbulence first occurs via a shear-layer instability above low-speed streaks. Farther downstream, high-intensity broadband fluctuations are observed in equivalent positions on secondary low-speed streaks.

1. Introduction

Boundary-layer transition from laminar to turbulent flow is an important unsolved problem in fluid mechanics. When transition in a two-dimensional boundary layer is triggered by an isolated roughness element, a turbulent wedge is formed. The vertex of the wedge is located downstream of the initiating roughness and the edges of the wedge spread laterally at an essentially constant angle. While turbulent wedges have been studied for decades, the mechanisms through which they spread are not yet fully understood. This work approaches this problem experimentally and considers the classical case of wedges generated in incompressible, zero-pressure-gradient flow.

Turbulent wedges were first visualized by Gregory & Walker (1956) using smoke and china clay. Schubauer & Klebanoff (1955) studied the lateral spreading and observed that wedges are composed of a 6.4° half angle turbulent core, surrounded by a 10.6° half angle intermittent region. These spreading angles are remarkably constant throughout the literature and are only slightly sensitivity to pressure gradient (Zhong *et al.* 2003) and surface treatments such as riblets (Strand & Goldstein 2011).

Gregory & Walker (1956) were the first to describe the initial stages of wedge formation. In

† Email address for correspondence: alex.rj.berger@gmail.com

the near field of the initiating roughness. Experimental (e.g., by Baker 1979) and numerical (e.g., by Rizzetta & Visbal 2007) studies confirm the basic flow topology: As the incoming boundary layer encounters a roughness element, spanwise vorticity associated with the undisturbed boundary layer is reoriented in the streamwise direction. This results in a horseshoe vortex with a pair of counter-rotating streamwise vortices that extend in the downstream direction. These redistribute streamwise momentum across the boundary layer and are responsible for the emergence of high- and low-speed streaks. Ergin & White (2006) observed that breakdown to turbulence occurs via a Kelvin–Helmholtz-like instability of the shear layers located above the low-speed streaks. This topology has been shown to be robust to changes in roughness geometry by Ye *et al.* (2016) using tomographic particle-image velocimetry (PIV). Direct numerical simulations by Suryanarayanan *et al.* (2019) provide a four-stage description of the entire process from a vorticity dynamics perspective. Although some near-field details may be affected by roughness height and shape, the process ultimately leads to a turbulent wedge that undergoes lateral spreading.

To understand why turbulent wedges spread at the angle at which they do, Gad-El-Hak *et al.* (1981) used dye visualization in a water channel. Injecting blue dye in the freestream and red dye at the roughness location, it was observed that lateral spreading due to turbulent mixing (red dye) is much lower than what is observed for the overall lateral wedge spreading (blue dye). This suggests that, in addition to turbulent mixing, there is a destabilization mechanism acting on the surrounding laminar flow which is responsible for the lateral growth of the wedge. Chu & Goldstein (2012) and Goldstein *et al.* (2017) used direct numerical simulation (DNS) and confirm spreading is due to destabilization at the edge of the wedge rather than turbulent mixing from the core region. To establish this, they artificially damped turbulence in the core of the wedge and observed essentially no effect on lateral spreading.

With or without core turbulence damped, the DNS shows a succession of stationary low-speed streaks along the edges of the wedge that Chu & Goldstein (2012) named “dog teeth”. They hypothesized these stationary streaks are pinned in place by the stationary streamwise vortices that originate from the roughness element and, subsequently, “the spanwise growth of the wedge is the result of the formation of a spanwise succession of streaks, where the formation of each, in turn, is the result of an instability introduced by the vorticity field preceding it upstream.” The streaks recur with a lateral spacing of approximately 120 wall units which corresponds to about $2.25 \delta_k^*$ of the surrounding laminar boundary layer. (δ_k^* is the boundary-layer displacement thickness at the roughness location.) Taking the wedge spreading angle to be 6° (which is supported by figure 2 in Goldstein *et al.* 2017), the streamwise spacing is about $21 \delta_k^*$.

Similar dynamics are observed on the flanks of turbulent spots. Using DNS, Brinkerhoff & Yaras (2014) observe a self-regenerating process through which a hairpin vortex at the edge of a spot generates a low-speed streak between its legs and a high-speed streak outboard of the spot. The high-speed streak stretches the spanwise boundary-layer vorticity in the streamwise direction and, subsequently, the streamwise vortex lines are lifted up over the high-speed streak. The stretched and lifted vortex lines collect into new child hairpin vortices outboard of the parent. In turn, these break down and lead to the emergence of new low- and high-speed streaks outboard of the preceding streak.

The succession of low-speed streaks has previously been observed in an experiment by Watmuff (2004) who generated a steady low-speed streak and excited it with high-frequency oscillations. The streak broke down to turbulence and, where it did, a pair of laterally displaced low-speed streaks were generated. The initial low-speed streak plus the displaced secondary pair were associated with laterally displaced high-speed streaks farther downstream. Based on this, Watmuff suggested that lateral spreading “is the result of the formation of a spanwise

succession of streaks, where the formation of each in turn is the result of an instability introduced by the streak immediately preceding it upstream.”

Inspired by the Chu & Goldstein (2012) DNS, Kuester & White (2016) undertook an experiment matched to the DNS conditions in an effort to observe that streaks are associated with lateral wedge spreading. Hotwire measurements paired with naphthalene shear stress visualization showed a pair of low-speed streaks generated by a discrete roughness element. These destabilized, became turbulent, and produced of a new pair of low-speed streaks laterally displaced outboard. Somewhat downstream of the low-speed streaks, a pair of high-speed streaks appears further out from the symmetry line. The high-speed streaks are the dog teeth observed in naphthalene flow visualization.[†]

A complementary experimental view is provided by a tomographic PIV study by Ye *et al.* (2016). Using measurements with $Re_{x,k} = 207 \times 10^3$ and $Re_{kk} = 1170$, Ye *et al.* observed small variations in wedge spreading angle, breakdown location, and streamwise streak spacing depending on roughness shape.[‡] Just behind the roughness, two pairs of counter-rotating streamwise vortices develop and a low-speed region along the symmetry line is unstable to strong Kelvin–Helmholtz-like vortices. Outboard of the central features, trailing legs of a horseshoe vortex are associated with stationary streamwise vorticity that generate low-speed flow on their upwash sides similar to the low-speed streak observation by Kuester & White (2016). Further downstream, high-speed streaks emerge further outboard where tertiary vortices produce downwash. Additional sets of streamwise vortices with alternating senses of rotation are also be observed. These measurements clearly show an alternating pattern of vortices lead to a repeating pattern of low-speed and high-speed streaks, exactly consistent with DNS results. Ye *et al.* report half angles of 6.4° , 5.5° , and 5.2° for cylinder, square, and hemisphere roughness, respectively. The distance from the first to second emergence of a low-speed streak is approximately $53 \delta_k^*$ for a cylindrical roughness and $74 \delta_k^*$ for a hemisphere, longer than the equivalent distances that can be inferred from the DNS results by Chu & Goldstein (2012).

Hotwire measurements by Kuester & White (2016) and Berger *et al.* (2017) give the frequency spectrum of velocity fluctuations at various locations in the flow. These confirm the findings by Ergin & White (2006) that roughness-induced transition occurs due to a high-frequency instability above and wrapping around the sides of low-speed streaks. These fluctuations are clearly associated with the unsteady vortices observed by Ye *et al.* (2016) and similar to those above the low-speed streaks in various DNS studies. To establish that breakdown results from an instability process, Berger *et al.* (2017) performed a linear-stability analysis of a two-dimensional slice of a low-speed streak as a basic state and found the most-unstable frequencies in good agreement with the measured fluctuation spectrum.

In addition to high-frequency fluctuations measured above low-speed streaks, Berger *et al.* (2017) measured low-frequency fluctuations on the sides of a low-speed streak. These were predicted by stability analysis but not observed in their companion DNS. When a control roughness was added to suppress transition, the high-frequency fluctuations were suppressed but the low-frequency fluctuations remained in the hotwire signals. Berger *et al.* interpreted these findings as evidence of low-frequency lateral meandering of the streak because lateral movement of a structure with $\partial U / \partial z$ shear would appear in hotwire measurements as u' fluctuations. The consequence of lateral meandering could be that time-averaged measurements along the edges of a turbulent wedge may fail to provide clear results. As ostensibly stationary structures meander, time-averaged signals at fixed points in the flow

[†] Chu & Goldstein (2012) use the term “dog teeth” for low-speed streaks but the naphthalene studies reveal high-speed streaks.

[‡] This $Re_{x,k}$ value is adjusted for the virtual leading edge using the Re_θ value at x_k quoted by Ye (2017).

would blur results from different flow regions. This possibility may explain why Kuester & White (2016) were unable to observe a successive pattern of streaks in their experiments. Ye *et al.* (2016) did observe a complete streak reoccurrence cycle in their data but the structures are not as clear downstream as upstream.

The long-standing observations of constant wedge spreading angles suggests a universal behavior. However, few experiments provide details about the mechanisms that drive lateral spreading. Previous experiments using roughness-initiated turbulent wedges have been performed at fixed and relatively low $Re_{x,k}$ and over relatively short streamwise distances. Experiments by Ye *et al.* (2016) were conducted at $Re_{x,k} = 207 \times 10^3$ over $132 \delta_k^*$ and experiments by Kuester & White (2016) were conducted at $Re_{x,k} = 541 \times 10^3$ over $116 \delta_k^*$. The spreading angle and streamwise streak spacing Ye *et al.* observed varied with roughness shape. And, the streamwise streak spacing was observed to be substantially longer than corresponding values seen by Goldstein and coworkers (Chu & Goldstein 2012; Goldstein *et al.* 2017) using DNS at higher $Re_{x,k}$. Kuester & White (2016) matched the DNS $Re_{x,k}$ value but did not observe a complete streak reoccurrence cycle so cannot provide spacing data for comparison.

To address the need for additional data, this work investigates the emergence of high- and low-speed streaks along the sides of multiple realizations of roughness-induced turbulent wedges over a range of $Re_{k,x}$ at three supercritical Re_{kk} values. Naphthalene shear stress visualizations are made for 17 separate turbulent wedges initiated at $Re_{x,k}$ values from 231×10^3 to 1.505×10^6 , which spans from the Reynolds numbers tested by Ye *et al.* (2016) to almost three times higher than the values tested by Kuester & White (2016). The measurement domain extends at least $78 \delta_k^*$ and up to $265 \delta_k^*$. The work by Ye *et al.* and Kuester & White extended only from $116 \delta_k^*$ to $132 \delta_k^*$. Extensive hotwire measurements of mean and fluctuating streamwise velocity are made at each of the Re_{kk} values. Of particular interest is the growth of fluctuations expected above the low-speed streak. The hotwire measurements are also examined for evidence of low-frequency streak meandering.

2. Experimental Approach

The experiments are performed using a flat plate model in the Klebanoff–Saric Wind Tunnel (KSWT) at Texas A&M University. The KSWT is a low-speed wind tunnel designed to produce minimal freestream turbulence and sound. The test section is $1.4 \text{ m} \times 1.4 \text{ m}$ and is 5 m long. The freestream turbulence intensity is $Tu = 0.02\%$ with a bandpass from DC to 10 kHz (Hunt *et al.* 2010). The sound pressure fluctuations higher than 30 Hz are 83.6 dB (Kuester & White 2012). These values were confirmed at the outset of the present experiments.

The flat plate spans the height of the test section and is 4.4 m long. It is composed of 1-mm -thick aluminum skins that cover a 20-mm -thick paper honeycomb core. The elliptic leading edge is 343-mm long. A set of adjustable mounting brackets provide constant pressure on the test side of the plate. Zero pressure gradient is confirmed using boundary-layer profile measurements at each operating unit Reynolds number. Measured shape factors $H = 2.59 \pm 0.04$ indicate the pressure gradient is suitably close to zero for stability experiments (Saric 2007). The same measurements provide the virtual leading edge, x_{vle} , of the Blasius boundary layer such that $\delta^* = 1.72[(x - x_{vle})/Re']^{1/2}$ where x is the actual distance from the leading edge.

The experiments study turbulent wedges generated by cylindrical roughness elements of the same design used by Kuester & White (2016) with $k/d = 1.05$. The larger roughness is $k = 2.94 \text{ mm}$ and $d = 2.79$; the smaller is $k = 1.96 \text{ mm}$ and $d = 1.86$. Both feature a 0.2 mm

$\times 0.2$ mm square notch used to intentionally break symmetry for matched DNS studies (e.g., Chu & Goldstein 2012). The notch is positioned in the $+z$ spanwise direction.

To provide a range of $Re_{x,k}$ values at the fixed Re_{kk} values, the roughness elements are located at various streamwise positions while the wind tunnel is operated at different unit Reynolds numbers, $Re' = U_\infty/\nu$, values ranging from $508 \times 10^3 \text{ m}^{-1}$ to $850 \times 10^3 \text{ m}^{-1}$. Streamwise locations are identified for both the larger and smaller roughness elements that provide the three Re_{kk} values: 600, 750, and 979. The freestream speed is automatically adjusted as temperature varies to maintain constant Re' . This keeps $Re_{x,k}$ and Re_{kk} constant for across long-duration runs and from day to day.

3. Naphthalene Wedge Geometry Survey

3.1. Naphthalene procedures and image analysis

Naphthalene shear-stress visualization is an effective method for rapid detection of the laminar/turbulent interface. It has been used in a variety of experiments in the KSWT ranging from those by Dagenhart *et al.* (1989) (when the tunnel was located at Arizona State University) to the studies by Kuester & White (2016) and Berger *et al.* (2017). The method consists of dissolving naphthalene in acetone and spraying a thin coating of the mixture onto the test surface. The acetone evaporates leaving behind a layer of milky white naphthalene crystals. When the tunnel is run, the naphthalene sublimates revealing the aluminum flat plate. Sublimation occurs more quickly in regions of higher shear stress. After several minutes, turbulent regions and then laminar regions with elevated shear stress are revealed as dark regions as opposed to the light-gray low-stress regions. Eventually, the naphthalene remaining in low-shear regions sublimates away leaving an entirely clear plate. Figure 1 is an example image in which several high-speed streaks can be seen extending upstream from the turbulent wedge.

Prior to naphthalene application, an image is taken of the flat plate with a calibration grid marked on its surface. This provides a reference for image distortion correction in processing software and to generate the pixel scale. Multiple photographs are collected as the naphthalene sublimates and these are analyzed to generate the data of interest. After image distortion is removed, geometrical parameters are manually extracted. Two points, one upstream and one downstream, are marked that best characterize the interface on both sides of the wedge. The wedge lines corresponding to figure 1 are shown in figure 2. The lines' angles relative to the flow direction are the wedge-spreading half angle and their intersection is the effective wedge origin. The distance from the roughness element center to the effective origin is denoted Δx_0 .

High-speed streaks are often seen to originate outboard of the main wedge edge. Their locations are marked as red dots in figure 2. They rarely occur at the same streamwise location on both sides of the wedge and are noted as separate locations, not an average. The origin of the most-upstream streak on either side of the wedge is recorded as a distance Δx_1 from the roughness center. The origin of the second streak high-speed streak is denoted Δx_2 and is referenced to the origin of the first streak on the same side of the wedge.

While naphthalene visualizations provide much data relatively quickly, there are difficulties extracting quantitative data from naphthalene images. First, it is impossible to provide a perfectly uniform coating and this can lead to regions of equivalent shear being revealed at different rates. Second, naphthalene edges are not exactly straight lines because of the high-speed streaks that emerge on the edges. For this reason, a strict protocol was implemented in order to extract the geometries from the images. From the multitude of pictures taken of

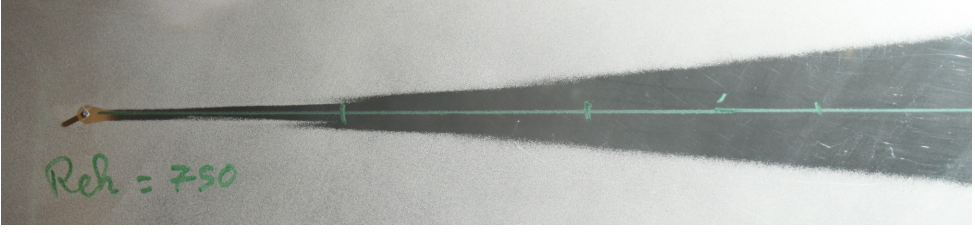


Figure 1: Example naphthalene image for $Re_{x,c} = 343 \times 10^3$ and $Re_{kk} = 750$.

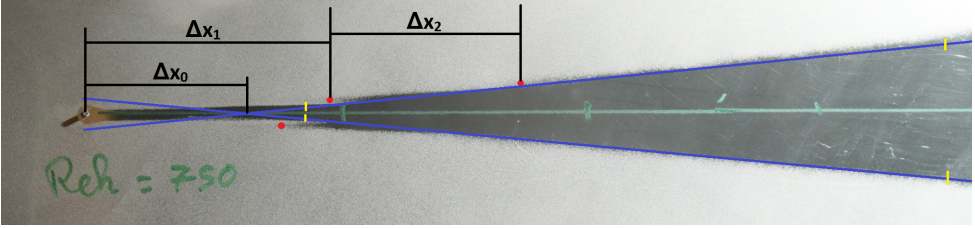


Figure 2: Wedge geometry analysis corresponding to figure 1

every turbulent wedge case, the image with the best contrast revealing the turbulent regions with no sublimation occurring in laminar regions is selected for analysis.

To efficiently cover the range of target $Re_{x,k}$ and Re_{kk} values, three roughness elements were placed on the flat plate at different spanwise positions and tested simultaneously. The elements were positioned so that the resulting wedges did not intersect until far downstream. Table 1 summarizes the various roughness positions, sizes, Reynolds numbers, and δ_k^* values. Also listed are the lengths, L , of the useful measurement range downstream of the element. The streamwise positions of the roughnesses are relative to the physical leading edge of the plate. The virtual leading edge lengths are accounted for in the Reynolds numbers and displacement thicknesses. Some of the Re' settings only include one or two roughnesses because those did not allow for effective additional measurements besides those listed.

3.2. Wedge spreading results

The working hypothesis is that Δx_0 and Δx_1 , the distances from the roughness element to the effective wedge origin and to the initial set of high-speed streaks, depend on roughness details so vary with both $Re_{x,k}$ and Re_{kk} . However, following the emergence and breakdown of the first set of streaks, wedge spreading is no longer affected by the instigating roughness. Thus, the wedge spreading angle and Δx_2 are expected to not depend on Re_{kk} .

Wedge-spreading half angles are plotted in figure 3. The data are shown with open symbols representing the $+z$ side of the wedge and filled symbols representing the $-z$ side. The mean spreading half angle is 5.7° with substantial scatter between 3° and 8° . No significant trend is visible in the data with respect to side of the wedge, $Re_{x,k}$, or Re_{kk} . Error bars are $\pm 0.25^\circ$ and represent the variability of repeated analysis of naphthalene images. Variability in the naphthalene coating is a much larger source of uncertainty but is not possible to quantify. Assuming there is no underlying trend in the data, the standard deviation of the half-angle data, 1.4° , represents the total half-angle uncertainty.

Results for Δx_0 , the distance from the roughness element to the virtual wedge origin, can be made nondimensional by Re' . Results in figure 4 show that $Re'\Delta x_0$ is constant across the range of $Re_{x,k}$ values tested, at least within the data scatter. The dashed lines are mean values for the $Re_{kk} = 600$ data and the combined $Re_{kk} = 750$ and 979 data. The two larger

$Re' [m^{-1}]$	$x_k [mm]$	$\delta_k^* [mm]$	$k [mm]$	$L [mm]$	$Re_{x,k}$	Re_{kk}	k/δ_k^*	L/δ_k^*
508×10^3	718	1.74	1.96	376	265×10^3	600	1.12	215
508×10^3	1255	2.45	2.94	500	523×10^3	979	1.20	204
550×10^3	878	1.93	1.96	512	380×10^3	600	1.02	265
550×10^3	607	1.50	1.96	326	231×10^3	750	1.30	217
550×10^3	1555	2.71	2.94	483	752×10^3	979	1.08	178
600×10^3	1102	2.14	1.96	425	554×10^3	600	0.92	199
600×10^3	750	1.68	1.96	345	343×10^3	750	1.17	205
600×10^3	1981	2.98	2.94	294	1082×10^3	979	0.99	99
650×10^3	1366	2.33	1.96	281	778×10^3	600	0.84	120
650×10^3	920	1.85	1.96	307	488×10^3	750	1.06	166
650×10^3	2485	3.25	2.94	253	1505×10^3	979	0.91	78
700×10^3	1676	2.53	1.96	553	1059×10^3	600	0.78	219
700×10^3	1180	2.07	1.96	261	712×10^3	750	0.95	126
750×10^3	2033	2.72	1.96	347	1407×10^3	600	0.72	128
750×10^3	1346	2.17	1.96	265	892×10^3	750	0.90	122
800×10^3	1607	2.32	1.96	265	1165×10^3	750	0.84	114
850×10^3	1902	2.47	1.96	272	1493×10^3	750	0.79	110

Table 1: Summary of wedge spreading test conditions.

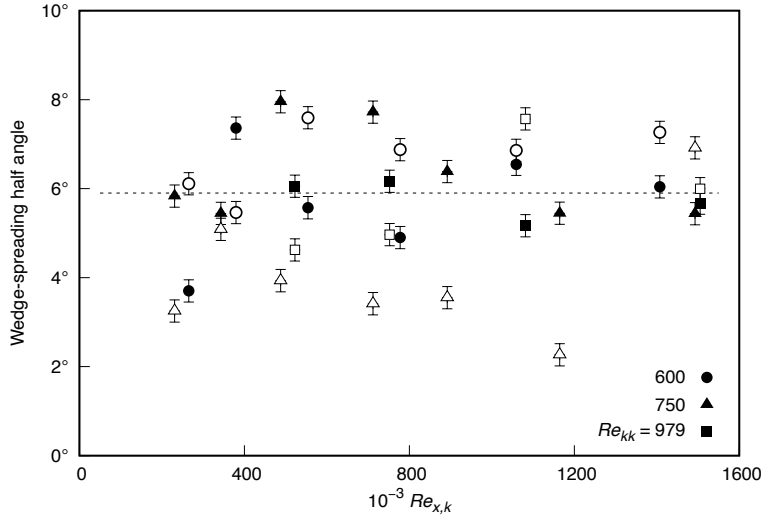


Figure 3: Turbulent wedge spreading half-angle. The dashed line indicates the mean spreading angle, 5.7° . Open symbols are angles measured on the $+z$ side of the wedge; filled symbols are the $-z$ side.

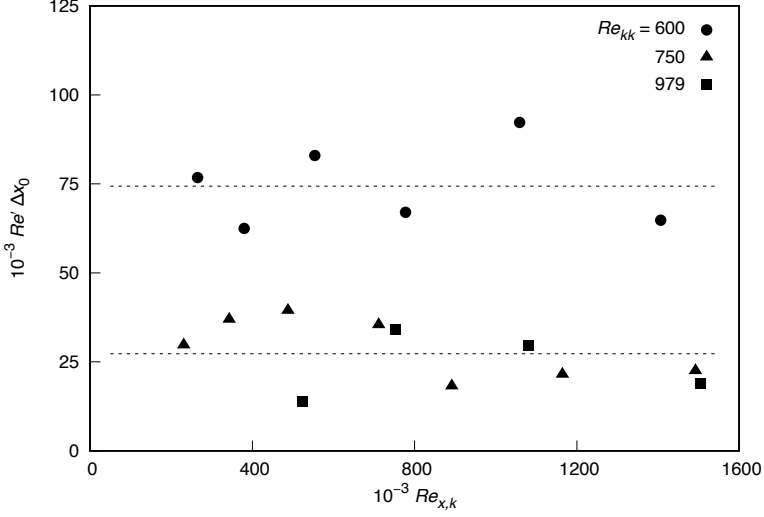


Figure 4: Turbulent wedge virtual origin distance times unit Reynolds number, $Re'\Delta x_0$.

Re_{kk} configurations have a mean of $Re'\Delta x_0 = 27 \times 10^3$ while the $Re_{kk} = 600$ mean is about three times larger, 74×10^3 . Because δ_k^* varies as $Re_{x,k}^{-1/2}$, the same data nondimensionalized as $\Delta x_0/\delta_k^*$ would show a decreasing number of boundary-layer thicknesses between the roughness and virtual wedge origin as $Re_{x,k}$ is increased.

The nondimensional distance from the roughness element to the most-upstream set of high-speed streaks, $Re'\Delta x_1$, is shown in figure 5. No sensitivity to $Re_{x,k}$ is observed. Similar to figure 3, open symbols are distances measured on the $+z$ side of the wedge and filled symbols are the $-z$ side. There does not appear to be a trend relating to which side of the wedge a high-speed streak first appears. (The roughness element notch is always positioned on the $+z$ side.) In several $Re_{kk} = 600$ cases, a streak was not observed on one side of the wedge in the naphthalene patterns so not all data have both $+z$ and $-z$ data. Similar to the Δx_0 data, the Δx_1 data is equivalent in the $Re_{kk} = 750$ and 979 cases while the initial high-speed streaks appear somewhat further downstream for $Re_{kk} = 600$. The two larger Re_{kk} values yield a combined mean of $Re'\Delta x_1 = 41 \times 10^3$ while the mean for $Re_{kk} = 600$ is about twice that, $Re'\Delta x_1 = 80 \times 10^3$. Comparing these values and figures 4 and 5 reveals that the initial high-speed streaks tend to appear just downstream of the virtual wedge origin.

Figure 6 shows the nondimensional distance between the first and second sets of high-speed streaks, $Re'\Delta x_2$. Again, there is some separation between the $Re_{kk} = 600$ results and the larger Re_{kk} results but no dependence on $Re_{x,k}$. The streak-to-streak spacing is $Re'\Delta x_2 = 132 \times 10^3$ for $Re_{kk} = 600$ and 75×10^3 for the larger Re_{kk} values. Especially considering the data scatter, these values are consistent with the results by Ye *et al.* (2016) who observed $Re'\Delta x_2 = 41 \times 10^3$ for a cylinder roughness and 58×10^3 for a hemisphere roughness at $Re_{kk} = 1170$ and $Re_{x,k} = 207 \times 10^3$.

Insensitivity of Δx_2 to Re_{kk} was expected but not observed. If wedge spreading is a universal phenomenon, $Re'\Delta x_2$ should not be affected by Re_{kk} . However, the data show that spacing to be approximately 1.75 times longer for $Re_{kk} = 600$ as compared to the larger-amplitude roughness cases. The ratio between different Re_{kk} values is less than that observed for $Re'\Delta x_0$ and $Re'\Delta x_1$ so subsequent high-speed streak spacing values might collapse to a universal value. A third high-speed streak was identified in two of the 17 wedges. However, besides being too small a sample to be meaningful, the streak origins were impossible to

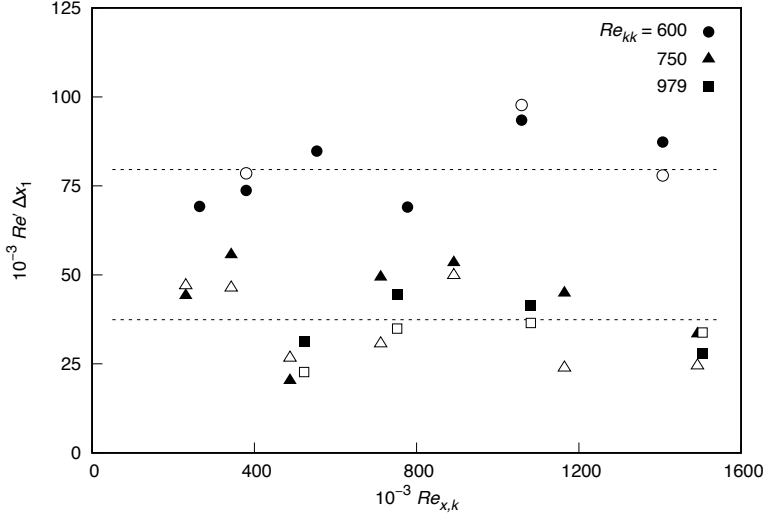


Figure 5: Initial high-speed streak position downstream of the roughness trip times unit Reynolds number, $Re' \Delta x_1$. Open symbols are distances measured on the $+z$ side of the wedge; filled symbols are the $-z$ side.

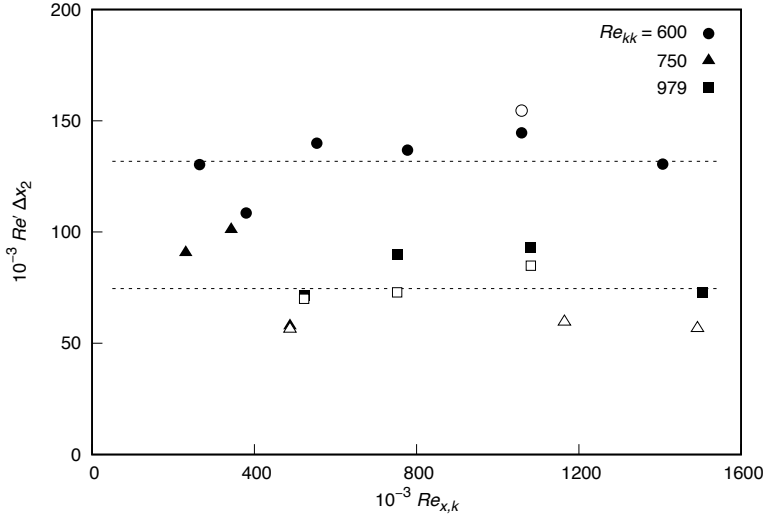


Figure 6: Distance between primary and secondary sets of high speed streaks times unit Reynolds number, $Re' \Delta x_2$. Open symbols are distances measured on the $+z$ side of the wedge; filled symbols are the $-z$ side.

locate with good accuracy. The reason for the difficulty is thought to be wedge meandering. This phenomenon is addressed below.

4. Hotwire Wedge Spreading Measurements

4.1. Hotwire measurement procedures

Hotwire measurements are made for three turbulent wedges corresponding to $Re_{kk} = 600$, 750, and 979. A summary of test conditions is given in table 2. For each wedge, measurements

Re_{kk}	k [mm]	d [mm]	Re' [m^{-1}]	x_{vle} [mm]
600	1.96	1.86	650×10^3	169 ± 12
750	1.96	1.86	750×10^3	157 ± 16
979	2.94	2.79	508×10^3	196 ± 12

Table 2: Summary of hotwire-measurement test conditions.

are made in wall-normal/lateral planes at multiple x locations. $Re_{kk} = 979$ was studied first and included 22 measurement planes extending from 5 mm to 165 mm downstream of the roughness element. $Re_{kk} = 600$ was studied second and featured a similar spacing but extended further downstream. The final $Re_{kk} = 750$ case included 48 measurement planes and increased resolution in the x and z directions. Data for the $Re_{kk} = 750$ case was collected over a period of seven weeks during which the hotwire data remained remarkably consistent.

Each measurement plane in a wedge includes between 21 and 81 boundary-layer profiles of the mean and fluctuating streamwise velocities, $U(y)$ and $u'(y, t)$. A 0.5-mm spanwise spacing is used where streaks are expected; a 1-mm spacing is used in the roughness near field; and 2 mm is used in the far field. Individual points are sampled for 2 seconds at 10 kHz. Each plane required between two and eight hours to measure.

To begin a boundary-layer profile measurement, a hotwire is positioned outside the boundary layer and moved toward the flat plate in progressively smaller steps. Each profile includes approximately 70 measurement points for laminar regions and 120 for turbulent regions. In the laminar region outside the wedge, measurements continue until the velocity reaches $0.12 U_\infty$. The linear portion of the velocity profile is used to calculate y_{wall} , the wall location as the point at which $U = 0$ would occur. Inside the wedge where the flow is turbulent, the wall shear is too large to use the same strategy and overshooting the wall location results in broken hotwires. To prevent this, laminar profiles are measured outside the wedge at the beginning of a run. The resulting y_{wall} positions are inputs to a quadratic fit of the wall position in the traverse-fixed coordinate system. As measurements are made in the turbulent region, the hotwire is moved to within 0.6 mm of the estimated wall location.

4.2. Wedge development overview

Results for the most-extensive data set, $Re_{kk} = 750$, are shown in figure 7. The near-field dynamics are similar to those observed by Kuester & White (2016) and Ye *et al.* (2016). Immediately downstream of the roughness element, a lobe of high-intensity fluctuations grow high in the boundary layer on the $z = 0$ centerline and breakdown to turbulence occurs rapidly. Separately, two low-speed streaks appear adjacent to the centerline behind the roughness. These streaks eventually lead to high-intensity fluctuations that break down around $x = 1390$ mm. A second set of low-speed streaks then appear outboard of the first set. The second set of low-speed streaks breaks down to turbulence around $x = 1470$ mm. Earlier hotwire measurements by Kuester & White (2016) and Berger *et al.* (2017) did not observe the emergence and breakdown of the second set of low-speed streaks. This is thought to be the first observation of the second set using hotwire anemometry that provides well-resolved fluctuation data.

A comparison of the naphthalene and hotwire results is given in figure 8. Hotwire velocity data are from 1.2 mm above the wall and are colored to indicate high or low velocity relative to the surrounding Blasius boundary layer. The central low-speed streak breaks down to turbulence first and leads to a high-speed streak. The low-speed flanking streaks

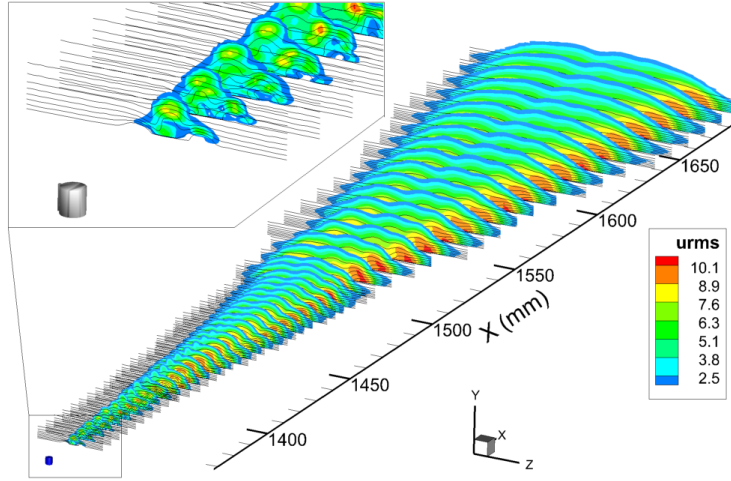


Figure 7: Measurements of the $Re_{kk} = 750$ turbulent wedge. Lines are iso-lines of mean velocity in 10% increments of U_∞ from 20% to 90%. Color contours indicate u'_{rms}/U_∞ levels that exceed 1.5%. The roughness trip is shown to scale at the lower left.

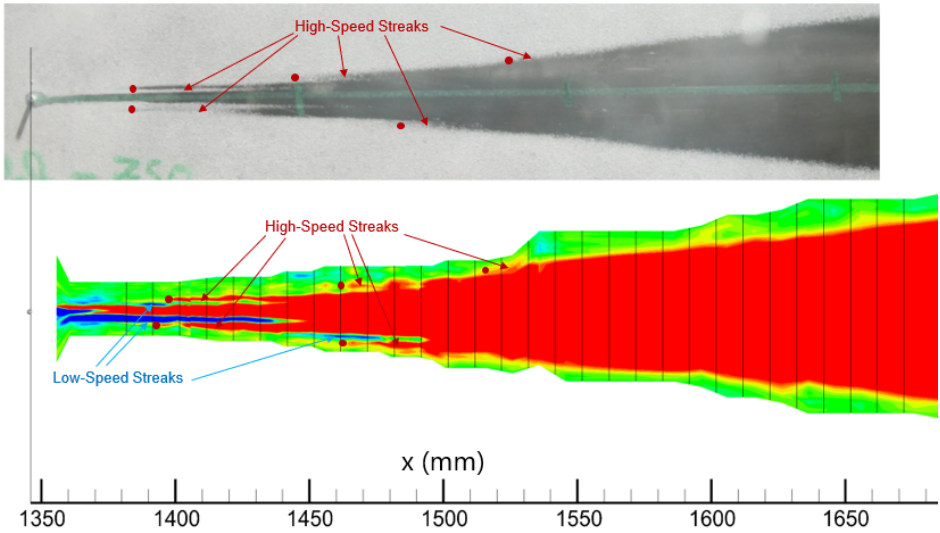


Figure 8: Comparison of naphthalene visualization and hotwire data for $Re_{kk} = 750$. Hotwire data is a plane at $y = 1.2$ mm. Color contours represent high (red) or low (blue) velocity relative to the surrounding Blasius boundary layer (green).

break down some distance later and produce high-speed streaks centered just outboard of the precipitating low-speed streaks. Red dots indicate where new high-speed streaks are judged to appear. Weaker low-speed streaks are observed outboard of the high-speed streaks and continue the cycle.

The naphthalene image and hotwire measurements shown in figure 8 were obtained during different parts of the test campaign and used different roughness applications. While great care was given to match flow conditions, streak breakdown is observed at somewhat different positions. Some of the differences may be attributable to small changes in the setup while

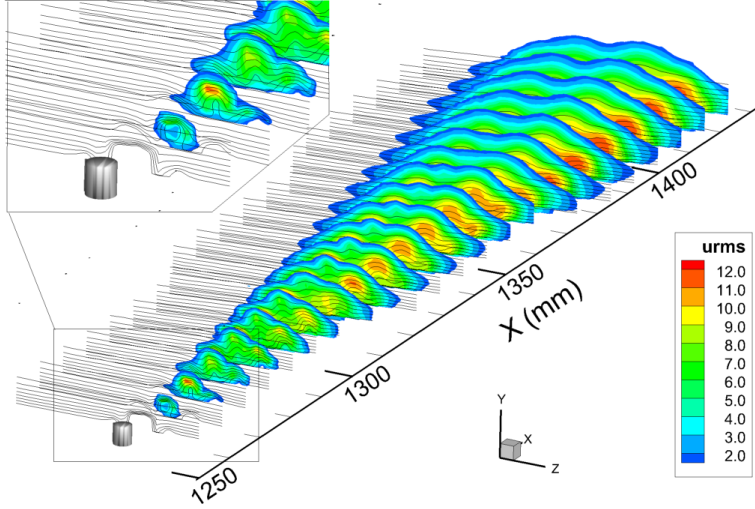


Figure 9: Measurements of the $Re_{kk} = 979$ turbulent wedge.

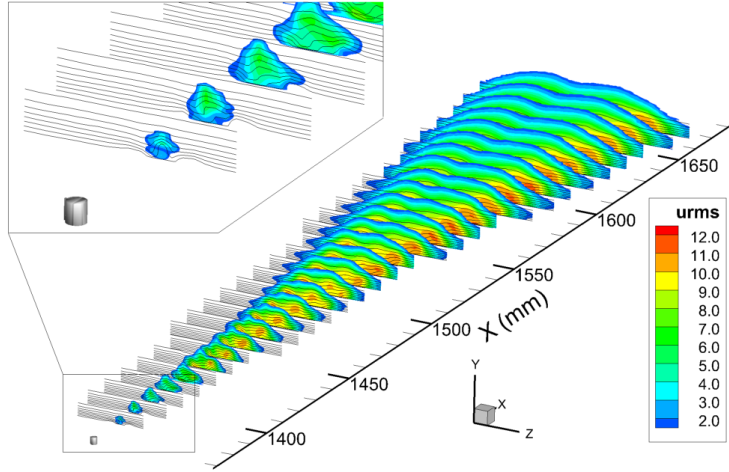


Figure 10: Measurements of the $Re_{kk} = 600$ turbulent wedge.

others to the different nature of the hotwire and naphthalene approaches. Nevertheless, the qualitative agreement between the methods is good.

Figure 9 for $Re_{kk} = 979$ shows very similar results to $Re_{kk} = 750$ and includes a central fluctuation lobe that breaks down to turbulence just aft of the roughness. Flanking low-speed streaks appear adjacent to the centerline and down around $x = 1310$ mm. A second set of low-speed streaks breaks down to turbulence around $x = 1390$ mm.

Figures 10 and 11 for $Re_{kk} = 600$ differ from the higher Re_{kk} values because breakdown does not occur on the $z = 0$ centerline just aft of the roughness element. Instead, breakdown occurs first on the flanking low-speed streaks near $x = 1450$ mm. Recalling figure 4, $Re_{kk} = 600$ configurations have substantially longer distances to the virtual wedge origin than the higher Re_{kk} cases. The hotwire data reveal the difference is due to the absence of breakdown in the immediate roughness wake for $Re_{kk} = 600$.

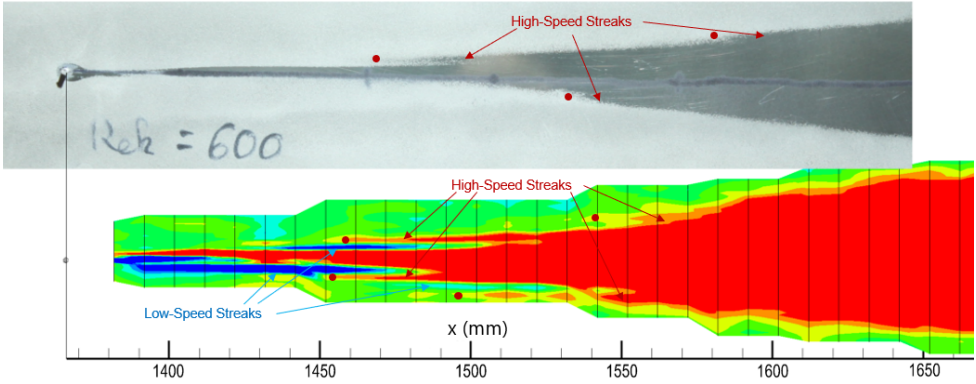


Figure 11: Comparison of naphthalene visualization and hotwire data for $Re_{kk} = 600$.

Once breakdown occurs for $Re_{kk} = 600$, it proceeds similarly as before. The flanking low-speed streaks support growing fluctuations that break down and lead to the cycle of recurring low- and high-speed streaks along the edges of the wedge. Two sets of high-speed streaks emerge in figure 11. The upstream set results directly from roughness element while the second set is the result of the repeating cycle of low- and high-speed streaks. The second set breaks down near $x = 1520$ mm. Moving downstream, no further distinct streaks are observed along the edges of the wedge. The absence of additional distinct streaks is thought to be the result of meandering that obscures measurements of further streaks.

4.3. Flanking streaks

The detailed progression of the streak breakdown cycle for $Re_{kk} = 750$ is presented in figures 12 and 13. Figure 12 shows the breakdown of the initial low-speed streaks that result directly from the roughness element while figure 13 shows the breakdown of the secondary streaks that arise from the wedge spreading mechanism. Breakdown on the $z = 0$ centerline has already occurred upstream of the plots shown in figure 12. The wedge is not perfectly symmetric and a stronger low-speed streak is observed on the $+z$ side. The description here will focus on the $+z$ side where the behaviors are more clear.

In figure 12, the data at $x = 1386$ mm, 40 mm downstream of the roughness trip, shows that the low-speed streak near $z = +4$ mm is very pronounced with strong shear in the y and z directions. Moving downstream, the shear layers relax but the upper region continues to support growing u'_{rms} fluctuations. By $x = 1416$ mm, high u'_{rms} levels reach to the wall on either side of the low-speed streak and a high-speed streak is forming outboard, around $z = +6.5$ mm. This recalls the pattern of high-speed streaks that arise outboard of the low-speed streaks in figures 8 and 11. Meanwhile, inboard of the low-speed streak, velocity contours are plunging toward the wall indicating high wall shear and the start of the turbulent wedge.

Further downstream at $x = 1431$ mm, figure 13 shows high-speed streaks with high-intensity u'_{rms} fluctuations on both sides of the low-speed streak at $z = +4$ mm. At $x = 1456$ mm, U iso-lines begin to lift up around $z = +10$ mm and form the second low-speed streak. This is more clearly visible at $x = 1471$ mm near $z = +9$ mm, 2.5 mm above the surface. Although the iso-lines in the middle of the boundary layer show a velocity deficit, naphthalene images would show this as a high-speed region because the near-wall iso-lines dip toward the wall. At this location, the iso-lines suggest a streamwise vortex with counterclockwise rotation. This corresponds exactly to the location and rotation of the “fourth

pair” streamwise vortex observed by Ye *et al.* (2016) using tomographic PIV downstream of a cylindrical roughness element. (See figure 5a in the paper by Ye *et al.*)

The progression of the highest u'_{rms} zone from $x = 1431$ mm to 1471 mm in figure 13 is noteworthy. At $x = 1431$ mm, there is a lobe of high-intensity u'_{rms} activity close to the wall that marks the high-speed streak at $z = +6.5$ mm. Moving downstream to $x = 1456$ mm, the fluctuation intensity associated with that high-speed streak decreases while a new zone of u'_{rms} activity appears higher in the boundary layer and slightly outboard as the new low-speed streak forms. Once again, the high fluctuation intensity is in the unstable region above the low-speed streak. Moving to $x = 1471$ mm, those high-intensity fluctuations are now wrapping around the low-speed streak at $z = +9$ mm in the same manner as at $x = 1416$ mm in figure 12. In this way, the progression of u'_{rms} fluctuation intensity can be used as a marker for low-speed and high-speed streak behavior, even where direct observation of streaks is difficult in time-average hotwire data and naphthalene images.

Still further downstream it becomes difficult to distinguish specific streak structures. In figure 14, the most upstream of the plots includes remnants of stationary low-speed and high-speed streaks in the core but these diminish in intensity as the wedge develops downstream. The highest u'_{rms} levels persist along the edges of the wedge.

4.4. Velocity fluctuation power spectra

An advantage of hotwire anemometry is the ability to measure well-resolved u' spectra and instability frequencies. Observations here focus on the region directly above the flanking low-speed streaks where fluctuations are associated with the wedge-spreading streak cycle. Fluctuation spectra for $Re_{kk} = 600$ are given in figure 15 corresponding to measurement locations shown in figure 16. At the most-upstream portion of the streak at $x = 1382$ mm (red), a band of unstable frequencies from around 500 to 900 Hz is identified. Moving downstream, the streak becomes more pronounced and there is rapid growth of the unstable band of frequencies, especially near 500 Hz. By $x = 1422$ mm (black) the flow has become locally turbulent with a broad u' spectrum.

The same behavior is observed in the low-speed streaks that form at $Re_{kk} = 750$ and 979. Data for $Re_{kk} = 979$ is shown in figure 17 for the locations indicated in figure 18. In this case, the unstable frequency band extends from around 300 to 600 Hz.† An important difference is the substantially increased fluctuation power at frequencies lower than the unstable band. This is thought to be a consequence of the turbulent breakdown on the $z = 0$ centerline that has already occurred by $x = 1270$ mm, the most upstream position pictured. Moving downstream, the breakdown of the low-speed streak happens in the same manner as for $Re_{kk} = 600$.

Fluctuation spectra and corresponding measurement locations for the second low-speed streak are presented in figures 19 and 20 for $Re_{kk} = 600$ and in figures 21 and 22 for $Re_{kk} = 979$. In both cases, the high-intensity turbulent fluctuations of the turbulent wedge obscure any unstable frequency bands that may exist at those locations. Nevertheless, regions of distinctly stronger fluctuations exist above the low-speed streaks.

The u'_{rms} contours show the highest-intensity fluctuations occur in the unstable shear layers above low-speed streaks and lead to breakdown along the flanks of the wedge. As noted previously, zones of high-intensity fluctuations may reveal the locations of low-speed streaks even when they might be obscured by meandering. To visualize these regions, the fluctuation power spectrum data is integrated across the unstable frequency band identified in the initial low-speed streak and iso-surfaces of the integrated power are then plotted to show the zones of highest-intensity velocity fluctuations in the wedge. Fluctuation iso-surfaces

† The frequency is lower than for the $Re_{kk} = 600$ case because of the lower freestream speed. See table 2.

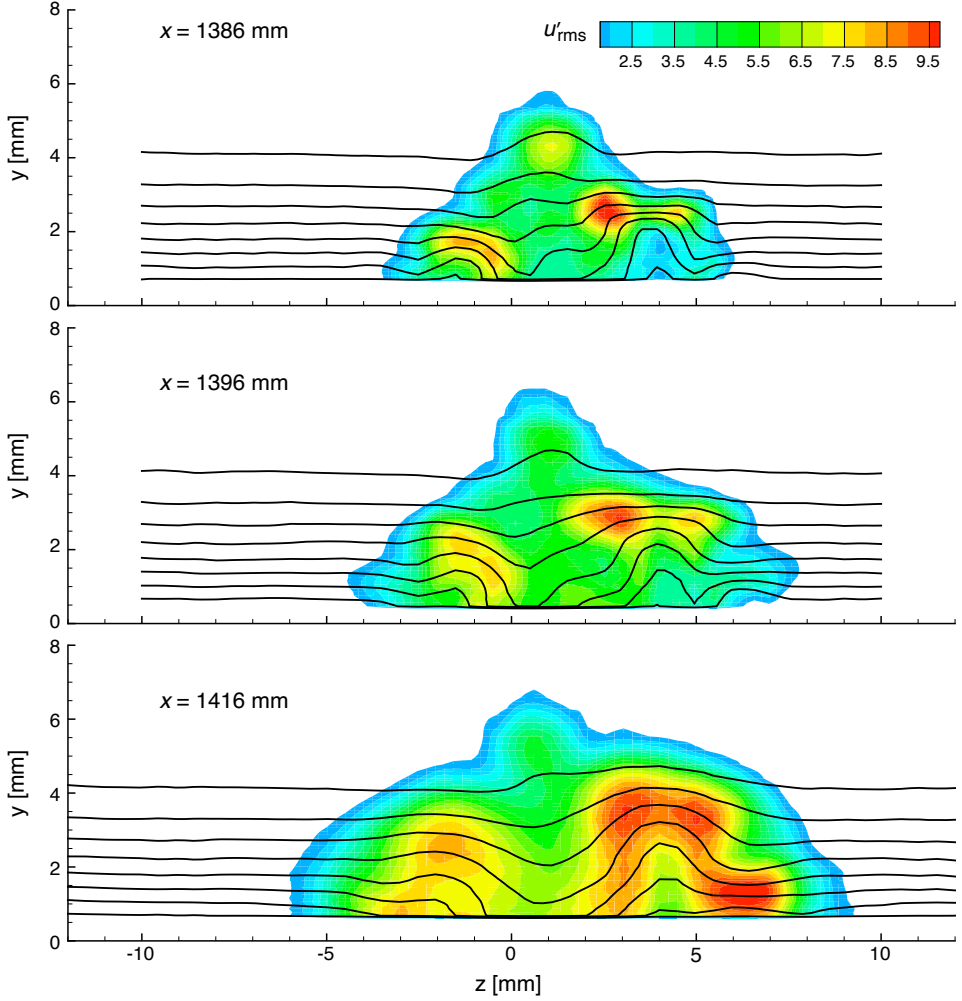


Figure 12: Measurements of the initial $Re_{kk} = 750$ low-speed streak cycle at $x = 1386$, 1396 , and 1416 mm. The roughness element is positioned at $x = 1346$ mm. Lines are iso-lines of mean velocity in 10% increments of U_∞ from 20% to 90%. Color contours indicate u'_{rms}/U_∞ levels that exceed 1.5%.

of the $Re_{kk} = 750$ data is presented in figure 23 and $Re_{kk} = 600$ data is presented in figure 24. The near-field behavior is clearly different between these cases and emphasizes the rapid breakdown on the $z = 0$ centerline when $Re_{kk} = 750$. As seen in previous figures, the $Re_{kk} = 600$ configuration breaks down much further downstream and does so first in the flanking low-speed streaks. $Re_{kk} = 979$ results are similar to $Re_{kk} = 750$. The iso-surfaces disappear at the downstream end of the $Re_{kk} = 750$ domain, potentially because meandering has spread the fluctuations across a larger spanwise range and thereby decreased the time-average intensity in the core of the high-fluctuation zone.

Figures 23 and 24 recall the DNS by Goldstein and co-workers (Chu & Goldstein 2012; Goldstein *et al.* 2017). Those simulations showed that wedge spreading is driven by activity along wedge edges even when the core turbulence is artificially damped. The current

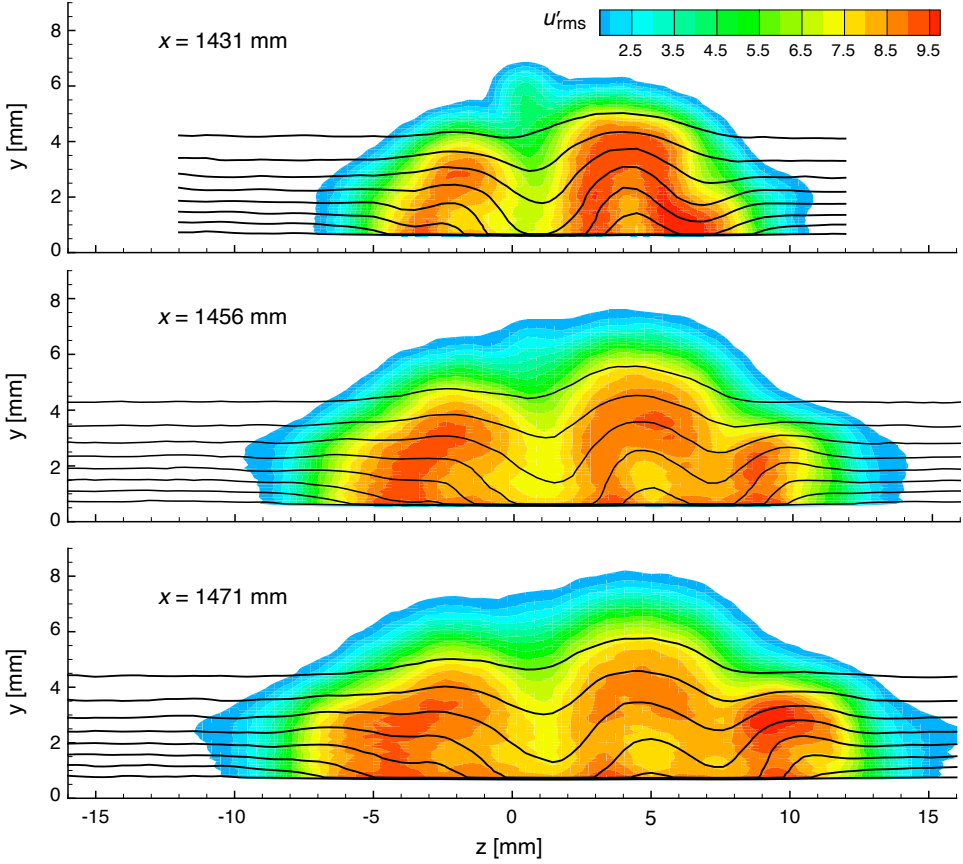


Figure 13: Measurements of the second $Re_{kk} = 750$ low-speed streak cycle at $x = 1431$, 1456 , and 1471 mm.

observation of highest-intensity fluctuations in the streak-instability band is consistent with that finding.

4.5. Streak meandering

It is hypothesized that streak meandering obscures the emergence, instability, and breakdown of streaks in the downstream portion of the turbulent wedge. Evidence for this was observed by Berger *et al.* (2017) who detected a low-frequency 60 Hz signal in the spanwise shear layers at the outer lateral edges of low-speed streaks. To investigate the possibility of streak meandering, a simple model of a low-frequency lateral oscillation of the wedge structure is considered. Figure 25 depicts the wedge-fixed reference frame in which a hotwire moves laterally with respect to a stationary streak. The key aspect of the model is that at different times, the hotwire is located in low-speed, high-speed, and crossing positions. The data show high-frequency fluctuations exist above low-speed streaks. In the meander model, this would associate higher-intensity high-frequency fluctuations with low-speed positions and lower-intensity high-frequency fluctuations with high-speed positions.

To test whether a correlation can be found between u' intensity and the low- or high-speed portion of a hotwire signal, the signal for each measurement point is segmented depending on whether the wire is judged to be in the low- or high-speed portion of the wedge. A bandpass filter is applied between 1 and 80 Hz and zero crossings of the filtered signal

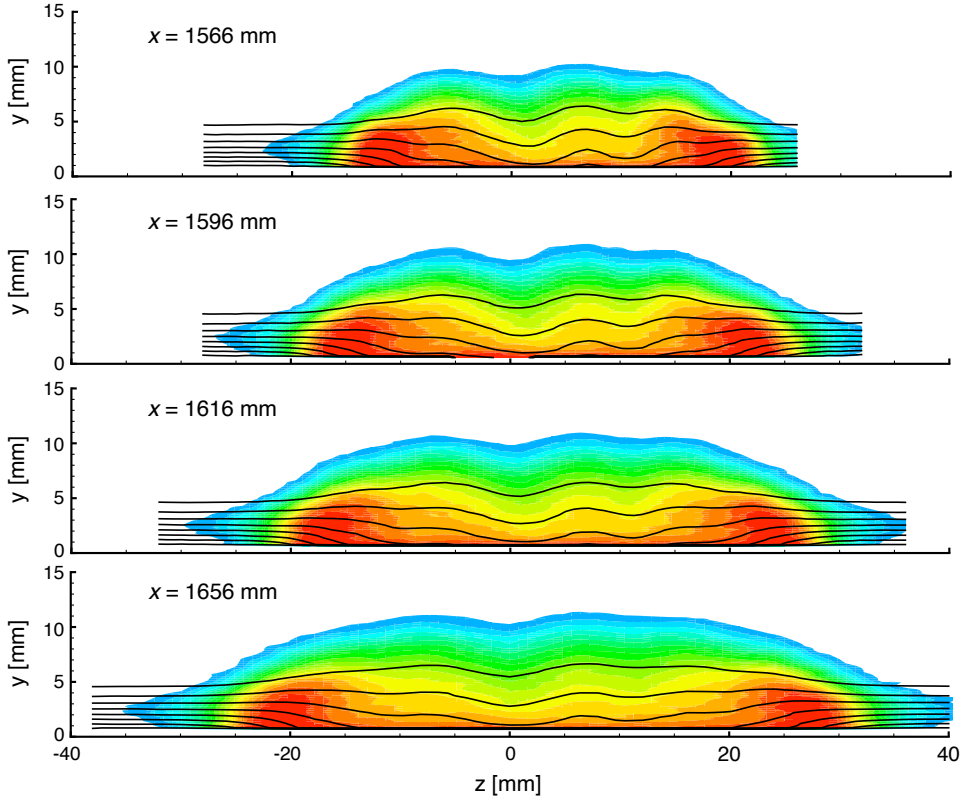


Figure 14: Measurements of the $Re_{kk} = 750$ wedge far downstream at $x = 1566, 1596, 1616,$ and 1656 mm.

are identified. An illustration is provided in figure 26. The u'_{rms} level of each segment is computed about the segment mean velocity then overall u'_{rms} values are computed for the high- and low-speed portions of the signal.

Figure 27 shows the difference between the low- and high-speed u'_{rms} signals for the $Re_k = 750$ case. $Re_{kk} = 600$ data are similar. $Re_k = 979$ data did not extend far enough downstream to provide meaningful results. Larger fluctuation amplitudes are observed in low-speed signal segments as compared to the high-speed segments, especially downstream on the edges of the wedge where low-speed streaks and their associated instabilities would exist. The far-field lateral regions of the turbulent wedge are where the effects of meandering are expected to be noticeable because the distance from the roughness that fixes the lateral position is the largest. Negligible differences are observed elsewhere. While this is not direct evidence of meandering, the data are consistent with what would be expected of a meandering wedge. This result supports the meandering hypothesis and may explain why secondary and subsequent streaks and their instabilities are difficult to capture in experiments.

5. Summary and Conclusion

These experiments seek to better elucidate turbulent wedge spreading using naphthalene flow visualizations and hotwire measurements. Turbulent wedges are initiated on a zero-pressure-gradient flat plate using supercritical cylindrical roughness elements with $Re_{kk} = 600, 750,$ and 979 . $Re_{x,k}$ values ranged from 231×10^3 to 1.505×10^6 , a much wider range than earlier

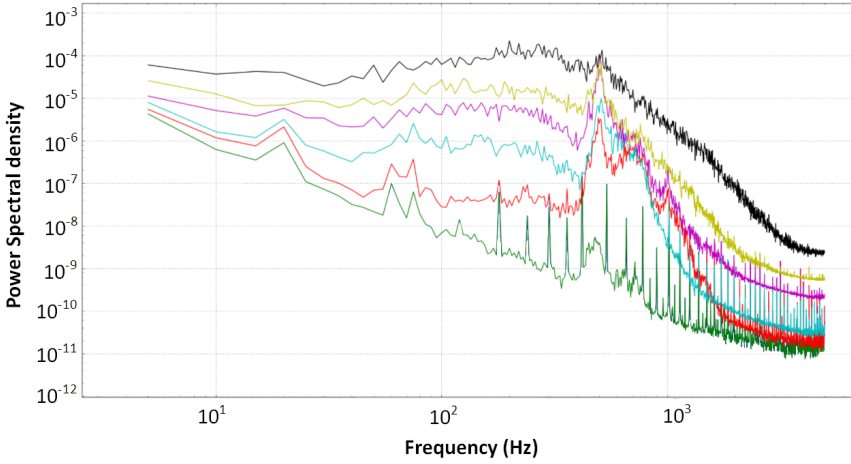


Figure 15: Velocity fluctuation power spectra in the initial low-speed streak for $Re_k = 600$. Spectra are color-coded corresponding to the locations indicated in figure 16.

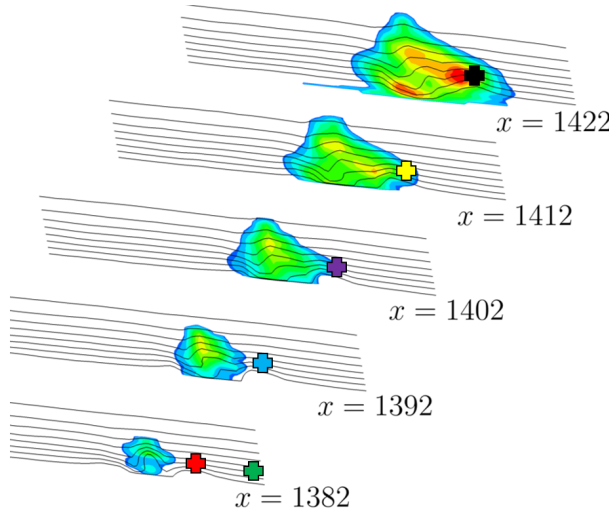


Figure 16: Locations of power spectra shown in figure 15.

studies and measurements are conducted over a substantially longer measurement domain. A key question this work seeks to answer is: What aspects of wedge spreading are universal and what aspects are sensitive to details of the roughness element? The working hypothesis is that the distance from the roughness to the virtual wedge origin, Δx_0 , and to the first occurrence of high-speed flanking streaks, Δx_1 , should depend on Re_{kk} . The spreading half angle and distance between successive streak origins, Δx_2 , are not expected to be affected by Re_{kk} because these measures begin well downstream of the initiating roughness. Another objective of the work is to document the instability and breakdown of low-speed streaks on the flanks of the turbulent wedges as this process appears to drive the lateral spreading of turbulent wedges.

The naphthalene flow-visualization survey reconfirms there is no apparent effect of $Re_{x,k}$ or Re_{kk} on the wedge-spreading half angle. A mean value of 5.7° was observed for the 17 naphthalene visualizations. This value is in good agreement with other experiments.

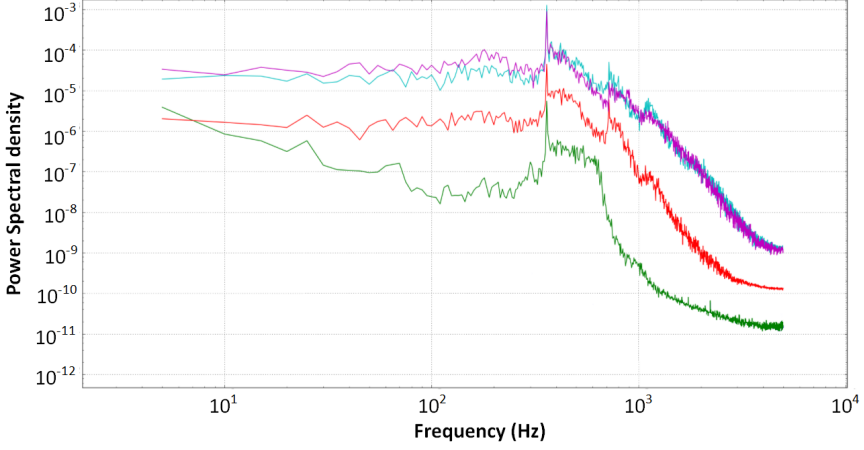


Figure 17: Velocity fluctuation power spectra in the initial low-speed streak for $Re_k = 979$. Spectra are color-coded corresponding to the locations indicated in figure 18.

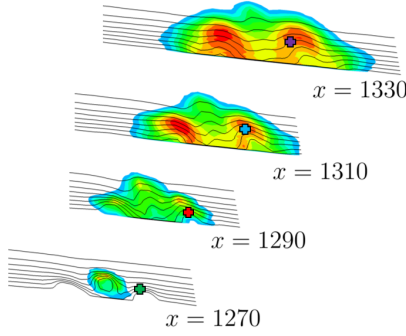


Figure 18: Locations of power spectra shown in figure 17.

When made nondimensional using Re' , the distance between the roughness and virtual wedge origin, $Re'\Delta x_0$, is not sensitive to $Re_{x,k}$ but does depend on Re_{kk} . The two larger Re_{kk} values, 750 and 979, gave equivalent results, $Re'\Delta x_0 = 27 \times 10^3$, while the mean for $Re_{kk} = 600$ is larger, 74×10^3 . The difference is explained by hotwire measurements that show initial breakdown to turbulence occurs high in the boundary layer just aft of the roughness element for the larger Re_{kk} configurations. At $Re_{kk} = 600$, breakdown occurs first in the low-speed flanking streaks, further downstream. That is, even for supercritical Re_{kk} values, there are different types of transition and which occurs affects the offset between the roughness element and the virtual wedge origin. Studies on the transition due to slightly subcritical roughness elements (e.g., Ergin & White 2006) correspond to longer $Re'\Delta x_0$ values, $Re_{kk} = 600$ is intermediate, and the $Re_{kk} = 750$ and 979 cases represent a high- Re_{kk} limit case. These results reveal the underlying dynamics of the Re_{kk} versus x -based transitions Reynolds number plots such as figure 10 by Klebanoff *et al.* (1992). The results for Δx_1 , the distance from the roughness to the first high-speed flanking streaks also show no sensitivity to $Re_{x,k}$. The two higher Re_{kk} cases give $Re'\Delta x_1 = 41 \times 10^3$ while $Re_{kk} = 600$ gives 80×10^3 .

The hypothesis that the streak-to-streak spacing is insensitivity to Re_{kk} was not confirmed. The data show that $Re'\Delta x_2 = 75 \times 10^3$ for the two higher Re_{kk} configurations and 132×10^3

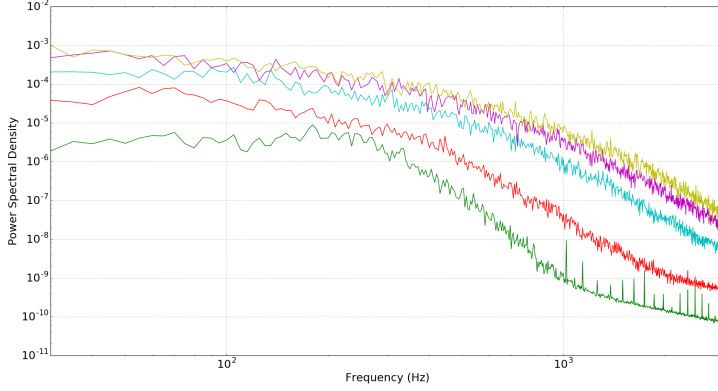


Figure 19: Velocity fluctuation power spectra in the second low-speed streak for $Re_k = 600$. Spectra are color-coded corresponding to the locations indicated in figure 20.

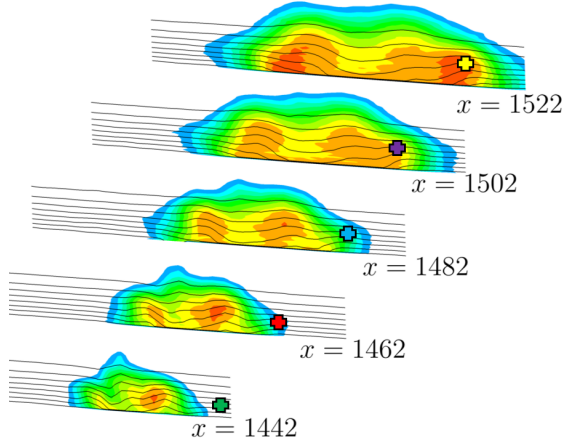


Figure 20: Locations of power spectra shown in figure 19.

for $Re_{kk} = 600$. A universal value of $Re' \Delta x_2$ would be consistent with a universal spreading angle so this is a somewhat surprising result. However, Ye *et al.* (2016) did observe different streak-to-streak spacings comparing cylindrical and hemispherical roughness elements; universality to roughness shape was also not observed in those experiments. In the present work, the difference between the high- and low- Re_{kk} values is less than for $Re' \Delta x_1$ so perhaps the spacing between subsequent streaks collapses to a universal value farther downstream. An insufficient number of further downstream streaks were observed to adequately address this possibility.

Extensive hotwire measurements were conducted and found in good agreement with the naphthalene visualization results. The measurements show that velocity fluctuations grow most strongly above low-speed streaks and break down to turbulence. Breakdown produces a high-speed streak immediately downstream of the initiating low-speed streak. Subsequently, a new low-speed streak is observed outboard of the high-speed streak and continues the wedge-spreading process.

Velocity spectra show u' fluctuations in a high-frequency band above the most-upstream

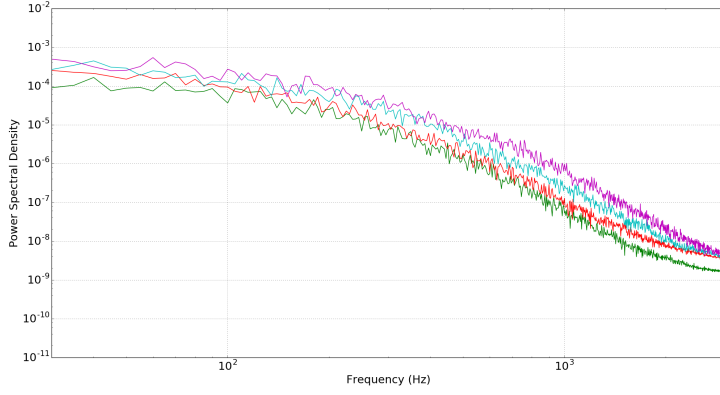


Figure 21: Velocity fluctuation power spectra in the second low-speed streak for $Re_k = 979$. Spectra are color-coded corresponding to the locations indicated in figure 22.

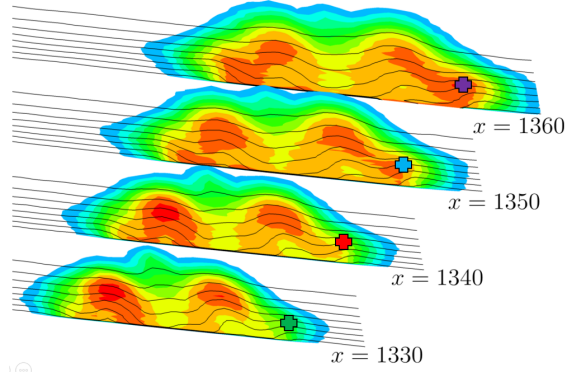


Figure 22: Locations of power spectra shown in figure 21.

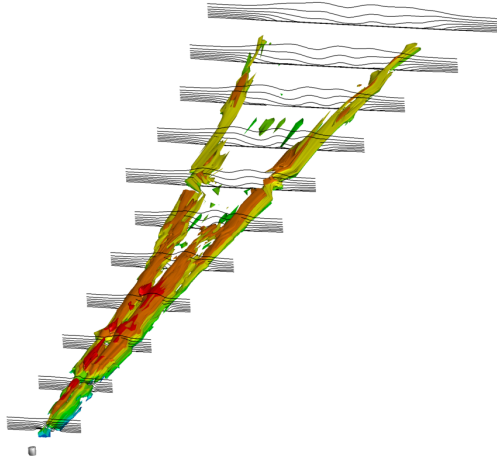


Figure 23: Iso-surfaces of u' fluctuation power in the streak-instability bandpass (arbitrary level) for $Re_{kk} = 750$. Surface colors indicate normalized velocity $U(y)$. Lines are iso-lines of mean velocity in 10% increments of U_∞ from 20% to 90%.

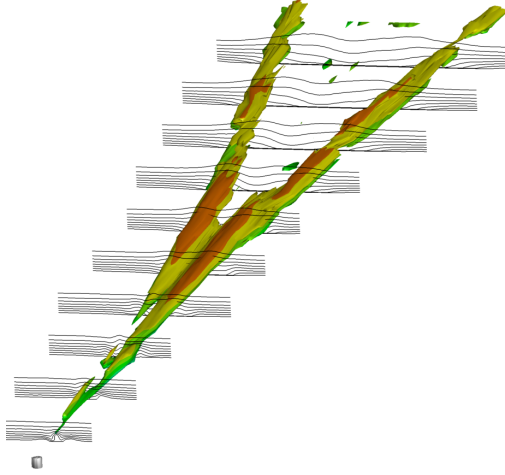


Figure 24: Iso-surfaces of u' fluctuation power in the streak-instability bandpass (arbitrary level) for $Re_{kk} = 600$.

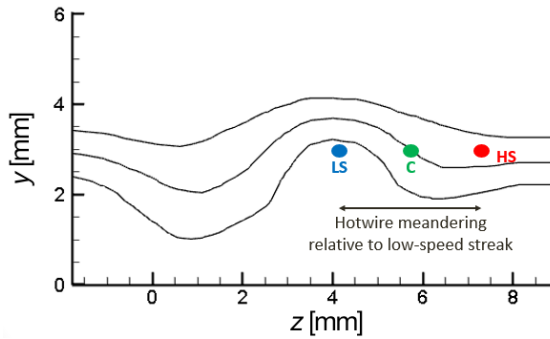


Figure 25: Streak meandering schematic. Hotwire positions LS (for low speed), C (crossing), and HS (high speed) are represented. In the experiment, the hotwire is fixed and the streak meanders relative to the sensor.

low-speed streak. Spectra obtained on subsequent streaks appear fully turbulent. The highest-intensity broadband u' signal exists in the same shear layers that supported the high-frequency instability of the more-upstream streaks. It is not clear why the spectra are broadband in the more downstream low-speed streaks, even at relatively low fluctuation intensities. There are several possibilities: Perhaps the nearby turbulent flow in the inner part of the wedge contaminates the nearby hotwire measurements by their strong fluctuations. Or, meandering is sufficiently strong that measurements above low-speed streaks are actually time averages of laminar, unstable zones and fully turbulent data. However, meandering is most pronounced far downstream and is unlikely to completely obscure unstable bands in the second set of low-speed streaks. A third explanation is that these regions are truly turbulent with highest-intensity u' fluctuations in the same upper shear layers as observed in the initial set of laminar low-speed streaks. If that is the case, the similarity between the process for the laminar low-speed streak and subsequent turbulent low-speed streaks would be reminiscent of the work by Gaster *et al.* (1985) who applied linear stability theory to a turbulent mixing layer with good agreement.

Continuing to resolve the cycle of low- and high-speed streaks that drives turbulent wedge

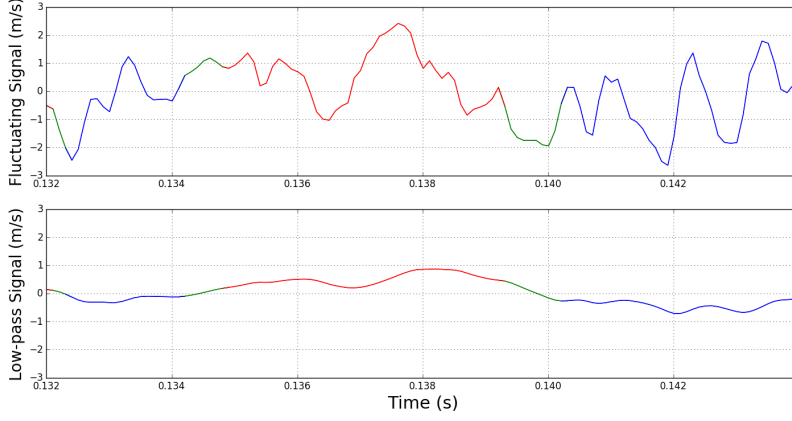


Figure 26: Signal separation example. Colors indicated the high-speed (red), crossing (green) and low-speed (blue) signal intervals.

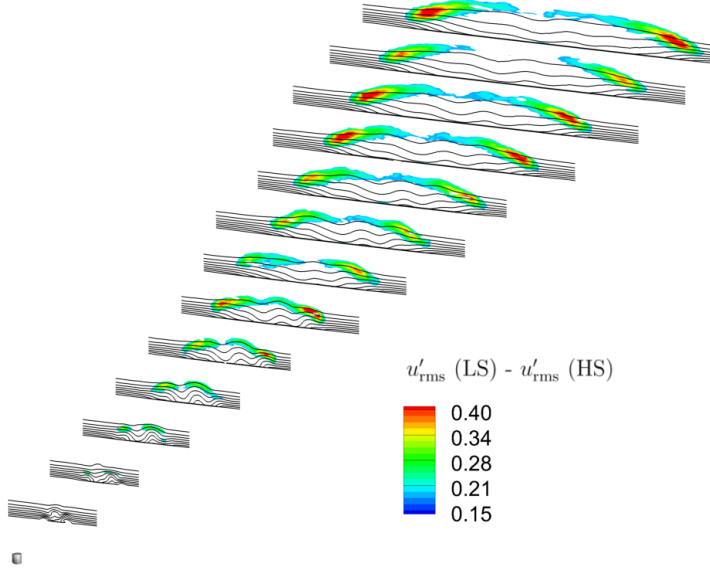


Figure 27: Difference between the velocity fluctuation levels of the low-speed and high-speed u'_{rms} signal components at $Re_k = 750$ (color scale). Normalized velocity contour lines from 0.2 to 0.9 with 10% increments.

spreading remains an important problem, particularly whether the streak-to-streak spacing, Δx_2 does eventually collapse to a universal value. Related to this, the laminar or turbulent character of low-speed flanking streaks remains an open question. Lateral meandering complicates progress on these issues. More sophisticated conditional averaging, perhaps using a reference sensor may be able to better resolve these questions.

Acknowledgements. The authors thank Dr D. Goldstein and Dr S. Suryanarayanan for fruitful discussions as well as Mr C. Finke for his assistance during the experiments.

Funding. This work was supported by the U.S. Air Force Office of Scientific Research through grant FA9550-15-1-0345.

Declaration of interests. The authors report no conflict of interest.

REFERENCES

- BAKER, CJ 1979 The laminar horseshoe vortex. *J. Fluid Mech.* **95** (2), 347–367.
- BERGER, ALEXANDRE R, McMILLAN, MADELINE N, WHITE, EDWARD B, SURYANARAYANAN, SAIKISHAN & GOLDSTEIN, DAVID B 2017 Suppression of transition behind a discrete roughness element using a downstream element. In *Proc. 10th Turbulence and Shear Flow Phenomenon Conference*.
- BRINKERHOFF, JOSHUA R. & YARAS, METIN I. 2014 Numerical investigation of the generation and growth of coherent flow structures in a triggered turbulent spot. *J. Fluid Mech.* **759**, 257–294.
- CHU, JEFF & GOLDSTEIN, DAVID 2012 Investigation of turbulent wedge spreading mechanism with comparison to turbulent spots. AIAA Paper 2012-0751.
- DAGENHART, J. RAY, STACK, J. PETER, SARIC, WILLIAM S. & MOUSSEUX, MARC C. 1989 Crossflow-vortex instability and transition on a 45 degree swept wing. AIAA Paper 89-1892.
- ERGIN, F GOKHAN & WHITE, EDWARD B 2006 Unsteady and transitional flows behind roughness elements. *AIAA J.* **44** (11), 2504–2514.
- GAD-EL-HAK, MOHAMED, BLACKWELDERF, RON F & RILEY, JAMES J 1981 On the growth of turbulent regions in laminar boundary layers. *J. Fluid Mech.* **110**, 73–95.
- GASTER, M., KIT, E. & WYGNANSKI, I. 1985 Large-scale structures in a forced turbulent mixing layer. *J. Fluid Mech.* **150**, 23–39.
- GOLDSTEIN, DAVID, CHU, JEFF & BROWN, GARRY 2017 Lateral spreading mechanism of a turbulent spot and a turbulent wedge. *Flow, Turbulence and Combustion* **98** (1), 21–35.
- GREGORY, N. & WALKER, W. S. 1956 The effect on transition of isolated surface excrescences in the boundary layer. *Tech. Rep. R. & M. 2779*. Aero. Res. Council.
- HUNT, LAUREN E., III, ROBERT S. DOWNS, KUESTER, MATTHEW S., WHITE, EDWARD B. & SARIC, WILLIAM S. 2010 Flow quality measurements in the Klebanoff–Saric wind tunnel. AIAA Paper 2010-4538.
- KLEBANOFF, P.S., CLEVELAND, W.G. & TIDSTROM, K.D. 1992 On the evolution of a turbulent boundary layer induced by a three-dimensional roughness element. *J. Fluid Mech.* **237**, 101–187.
- KUESTER, MATTHEW S. & WHITE, EDWARD B. 2012 Acoustic forcing and control of reflected waves in the Klebanoff–Saric wind tunnel. AIAA Paper 2012-2862.
- KUESTER, MATTHEW S & WHITE, EDWARD B 2016 Structure of turbulent wedges created by isolated surface roughness. *Experiments in Fluids* **57** (4), 47.
- RIZZETTA, DONALD P & VISBAL, MIGUEL R 2007 Direct numerical simulations of flow past an array of distributed roughness elements. *AIAA J.* **45** (8), 1967–1976.
- SARIC, WILLIAM S. 2007 Boundary-layer stability and transition. In *Springer Handbook of Experimental Fluid Mechanics* (ed. Cameron Tropea, Alexander L. Yarin & John F. Foss), pp. 886–896. Springer Berlin Heidelberg.
- SCHUBAUER, GALEN B & KLEBANOFF, PHILIP S 1955 Contributions on the mechanics of boundary-layer transition. *Tech. Rep. 3489*. National Advisory Committee for Aeronautics.
- STRAND, JAMES S & GOLDSTEIN, DAVID B 2011 Direct numerical simulations of riblets to constrain the growth of turbulent spots. *J. Fluid Mech.* **668**, 267–292.
- SURYANARAYANAN, SAIKISHAN, GOLDSTEIN, DAVID B & BROWN, GARRY L 2019 Roughness induced transition: A vorticity point of view. *Physics of Fluids* **31** (2), 024101.
- WATMUFF, JH 2004 Evolution of a turbulent wedge from a streamwise streak. In *Proc. 15th Australian Fluid Mech. Conf., Sydney, Australia*.
- YE, QINGQING 2017 Mechanisms of boundary layer transition induced by isolated roughness. PhD thesis, Technical University of Delft.
- YE, QINGQING, SCHRIJER, FERRY FJ & SCARANO, FULVIO 2016 Geometry effect of isolated roughness on boundary layer transition investigated by tomographic piv. *Intl. J. of Heat and Fluid Flow* **61**, 31–44.
- ZHONG, S, CHONG, TP & HODSON, HP 2003 A comparison of spreading angles of turbulent wedges in velocity and thermal boundary layers. *ASME J. Fluids Eng.* **125** (2), 267–274.